Clear and cloudy sky infrared brightness temperature assimilation using an ensemble Kalman filter

Jason A. Otkin[1]

Received 22 December 2009; revised 16 March 2010; accepted 30 March 2010; published 7 October 2010.

[1] A regional-scale Observation System Simulation Experiment was used to examine how the assimilation of window infrared brightness temperatures for both clear-sky and cloudy sky conditions impacts the accuracy of atmospheric analyses at convection-permitting scales when using an ensemble Kalman filter data assimilation system. The case study tracked the evolution of a large extratropical cyclone and associated cloud features across the central United States during 4–5 June 2005. Overall, the assimilation results revealed that the infrared brightness temperatures had a large positive impact on the simulated cloud field with the best results achieved when both clear-sky and cloudy sky observations were assimilated. The infrared brightness temperatures substantially reduced the bias and root mean square error in the cloud top pressure, cloud water path, 6.95 and 11.2 μm brightness temperatures, and vertical profiles of cloud condensate. Inspection of the thermodynamic variable statistics showed that the assimilation of conventional surface and upper-air observations produced more accurate temperature and wind analyses. When both cloud-affected and thermodynamic variables are considered, however, the best analysis was achieved when conventional observations and clear-sky and cloudy sky 8.5 μm brightness temperatures were assimilated simultaneously.

Citation: Otkin, J. A. (2010), Clear and cloudy sky infrared brightness temperature assimilation using an ensemble Kalman filter, *J. Geophys. Res.*, *115*, D19207, doi:10.1029/2009JD013759.

1. Introduction

[2] Clouds cover a substantial portion of the Earth's surface and exert a strong influence on the sensible weather through their effect on the surface temperature and by producing precipitation. The generation of accurate and spatially representative initial conditions within cloudy regions of the atmosphere suitable for numerical weather prediction is perhaps the most challenging aspect of modern data assimilation systems. Cloud processes are inherently nonlinear with complex interactions occurring between different hydrometeor species and the local thermodynamic environment at spatial scales far smaller than those present in most numerical models. Though cloud microphysical parameterization schemes have become more sophisticated in recent years, model errors continue to be large within cloudy regions. The strong correspondence between clouds and regions of rapid error growth suggests that a better utilization of both direct and indirect cloud observations has the potential to substantially improve forecast skill by producing a more accurate specification of the initial state within cloudy regions.

[3] Remotely sensed satellite observations of the outgoing radiation at the top of the atmosphere are the only reliable source of cloud data available on a near global scale. Advanced sensors onboard existing (and future) satellite platforms provide accurate radiance and reflectance measurements in dozens to thousands of visible, infrared, and microwave spectral bands, which together provide a wealth of detailed information about cloud properties and cloud extent. Clear-sky radiance measurements are also important since they provide critical information about the temperature and water vapor structure surrounding cloudy areas. For cloud-resolving data assimilation, observations from a geosynchronous platform are especially useful since their high temporal resolution and consistent spatial mapping of the same viewing area is able to more easily constrain rapidly changing cloud properties and modify the larger-scale dynamics that control cloud morphology [*Vukicevic et al.*, 2006; *Errico et al.*, 2007].

[4] Many prior studies have shown that the assimilation of infrared and microwave radiances and satellite-derived temperature and water vapor profile retrievals for clear-sky pixels has a large positive impact on the forecast skill especially where conventional observations are scarce, such as over the ocean and across the Southern Hemisphere [e.g., *Tracton et al.*, 1980; *Halem et al.*, 1982; *Andersson et al.*, 1991; *Mo et al.*, 1995; *Derber and Wu*, 1998; *McNally et al.*, 2000; *Bouttier and Kelly*, 2001; *Chevallier et al.*, 2004; *McNally et al.*, 2006; *Le Marshall et al.*, 2006; *Xu et al.*, 2009; *McCarty et al.*, 2009; *Collard and McNally*, 2009]. Until recently, most of the attention from the operational and research communities has been directed toward

[1]Cooperative Institute for Meteorological Satellite Studies, University of Wisconsin-Madison, Madison, Wisconsin, USA.

0148-0227/10/2009JD013759

extracting greater information from clear-sky observations since the assimilation of cloud-affected radiances poses a significant scientific challenge due to the presence of non-Gaussian error statistics and nonlinear cloud processes. Although more accurate initial conditions within clear areas will affect the evolution of nearby cloudy regions during the model integration, the assimilation of cloudy observations is necessary to further improve forecast skill within these regions.

[5] Recent studies by *Vukicevic et al.* [2004] and *Vukicevic et al.* [2006] have shown that cloudy infrared radiances assimilated using a 4DVAR data assimilation system improved the 3-D cloud structure in cloud-resolving model simulations provided that clouds were already present in the background field. Short-term forecast skill also increased with more frequent assimilation producing the best results. For a longer-term study employing a global circulation model, *Reale et al.* [2008] found that the forecast skill was much higher during the midlatitude winter when temperature retrievals from the Advanced Infrared Sounder (AIRS) were assimilated for both clear and partly cloudy conditions. Monte Carlo experiments within a 1DVAR framework have shown that temperature and humidity profiles are more accurate above the cloud top, particularly for cases containing midlevel clouds, when cloudy infrared radiances are assimilated [*Heillette and Garand*, 2007]. Encouraging results have also been achieved by extending the 4DVAR analysis control vector to include parameters such as cloud top pressure and cloud fraction and then simultaneously estimating these parameters along with temperature and humidity profiles inside the main 4DVAR analysis step [*McNally*, 2009]. *Zupanski et al.* [2010] recently used sensitivity tests to examine the potential benefit of assimilating cloudy infrared radiances within an ensemble-based assimilation system. Overall, their results indicate that the structure of the simulated cloud field improved after assimilation especially when all of the radiatively active hydrometeor species in the microphysics parameterization scheme are included in the control vector.

[6] In this study, results from a regional-scale Observation System Simulation Experiment (OSSE) will be used to examine how the assimilation of infrared brightness temperatures (which will be used interchangeably with "radiances") for both clear and cloudy sky conditions impacts the accuracy of atmospheric analyses at convection-permitting scales. Simulated observations from the Advanced Baseline Imager (ABI) to be launched onboard the Geosynchronous Operational Environmental Satellite (GOES)-R in 2016 will be employed. The ABI is a 16-channel imager containing 2 visible, 4 near infrared, and 10 infrared channels. Accurate radiance and reflectance measurements will provide detailed information about surface and cloud top properties, atmospheric water vapor, sea surface temperature, and aerosol and trace gas components with high spatial and temporal resolution [*Schmit et al.*, 2005]. The ensemble Kalman filter (EnKF) assimilation methodology [*Evensen*, 1994] will be used since unlike variational methods it is able to handle complex nonlinear microphysical processes in both the assimilation model and the forward observation operator and also provides a time-varying estimate of the background error covariance matrix used during the assimilation step. The paper is organized as follows. Section 2 contains a description of the data assimilation system with an overview of the case study provided in section 3. Results are shown in section 4 with conclusions presented in section 5.

2. Experimental Design

2.1. Forecast Model

[7] Version 3.0 of the Weather Research and Forecasting (WRF) model was used for this study. WRF is a sophisticated numerical weather prediction model that solves the compressible nonhydrostatic Euler equations cast in flux form on a mass-based terrain-following vertical coordinate system. Prognostic variables include the horizontal and vertical wind components, various microphysical quantities, and the perturbation potential temperature, geopotential, and surface pressure of dry air. High-resolution global data sets are used to initialize the model topography and other static surface fields. A complete description of the WRF modeling system is contained in the work of *Skamarock et al.* [2005].

2.2. Data Assimilation System

[8] Assimilation experiments were conducted using the EnKF algorithm implemented in the Data Assimilation Research Testbed (DART) data assimilation system developed at the National Center for Atmospheric Research [*Anderson et al.*, 2009]. The assimilation algorithm is based on the ensemble adjustment Kalman filter described by *Anderson* [2001], which processes a set of observations serially and is mathematically equivalent to the ensemble square root filter described by *Whitaker and Hamill* [2002]. DART includes tools that automatically compute temporally and spatially varying covariance inflation values during the assimilation step [*Anderson*, 2007, 2009]. To reduce sampling error due to a small ensemble size, covariance localization [*Mitchell et al.*, 2002; *Hamill et al.*, 2001] is performed using a compactly supported fifth-order correlation function following *Gaspari and Cohn* [1999].

2.3. Satellite Radiance Observation Operator

[9] A forward radiative transfer model used to compute simulated infrared brightness temperatures was implemented in DART. For each ensemble member, several steps are necessary to compute the simulated brightness temperature corresponding to a given observation. First, CompactOPTRAN, which is part of the National Oceanic and Atmospheric Administration's Community Radiative Transfer Model (CRTM), is used to compute gas optical depths for each model layer using simulated temperature and water vapor mixing ratio profiles and climatological ozone data. Ice cloud absorption and scattering properties, such as extinction efficiency, single-scatter albedo, and full scattering phase function, obtained from the work of *Baum et al.* [2006] are subsequently applied to each frozen hydrometeor species (i.e., ice, snow, and graupel) included in the model state vector. A lookup table based on Lorenz-Mie calculations is used to assign the properties for the cloud water and rainwater species. Visible cloud optical depths are calculated separately for the liquid and frozen hydrometeor species following the work of *Han et al.* [1995] and *Heymsfield et al.* [2003], respectively, and then converted into infrared cloud optical

depths by scaling the visible optical depths by the ratio of the corresponding extinction efficiencies. The surface emissivity over land is obtained from the *Seeman et al.* [2008] global emissivity data base, whereas the water surface emissivity is computed using the CRTM Infrared Sea Surface Emissivity Model. Finally, the simulated skin temperature and atmospheric temperature profiles along with the layer gas optical depths and cloud scattering properties are input into the Successive Order of Interaction (SOI) forward radiative transfer model [*Heidinger et al.*, 2006], which is used to compute the simulated brightness temperature. Previous studies by *Otkin and Greenwald* [2008] and *Otkin et al.* [2009] have shown that the forward model produces realistic infrared brightness temperatures for both clear-sky and cloudy sky conditions. *O'Dell et al.* [2006] have also shown that at microwave wavelengths the SOI model is accurate to within 1 K for a full range of atmospheric conditions. Due to generally less scattering, the accuracy of the SOI is also expected to be within 1 K at infrared wavelengths.

2.4. Simulated Observations

[10] To examine the impact that infrared brightness temperatures have on the analysis accuracy relative to conventional observations, simulated observations were produced for the ABI sensor and three conventional observing systems, including radiosondes, surface observations from the Automated Surface Observing System (ASOS), and pilot reports from the Aircraft Communications Addressing and Reporting System (ACARS). All simulated observations were computed using data from the high-resolution "truth" simulation to be described in section 3. To improve the realism of the OSSE results, special attention was given to ensuring that each observing system data set contains the correct spatial distribution with realistic measurement errors based on a given sensor's error specification randomly added to each observation. Simulated 8.5 μm infrared brightness temperatures were calculated using the SOI radiative transfer model and then interpolated to a representative ABI projection containing the correct horizontal resolution at all satellite zenith angles. The data were subsequently averaged to a resolution of ~60 km prior to assimilation. Simulated 2 m temperature and relative humidity observations were computed at existing ASOS station locations, whereas vertical profiles of temperature, relative humidity, and horizontal wind speed and direction were produced for each upper air station location. Given the importance of radiosonde observations, standard reporting conventions were followed so that each profile contains not only mandatory level data but also significant level data corresponding to features such as temperature inversions and rapid changes in wind speed and direction. Lastly, simulated ACARS temperature and wind observations were produced at the same locations as the real pilot reports listed in the Meteorological Assimilation Data Ingest Files (MADIS) for the OSSE case study period.

[11] The observation errors for the conventional observations were based on those found in the operational observation data set from the National Center for Environmental Prediction (NCEP). For the ASOS observations, the error was set to 2 K for temperature and 18% for relative humidity. Errors of 1.8 K and 3.8 m s^{-1} were used for the ACARS temperature and wind observations. The radiosonde errors varied with height and ranged 0.8–1.2 K for temperature, 1.4–3.2 m s^{-1} for the horizontal wind, and 20%–25% for relative humidity. Lastly, the observation error was set to 10 K for the simulated 8.5 μm brightness temperatures, which accounts for uncertainty in the forward model calculations, such as those associated with ice optical properties and scattering, as well as model and representativeness errors. Sensitivity tests using observation errors of 7.5 and 15 K, respectively, showed that the optimal results were achieved when the error was set to 10 K. The observation error covariance for each observation type was assumed to be diagonal.

3. Truth Simulation

[12] A high-resolution truth simulation tracking the evolution of a large extratropical cyclone across the central United States was performed using version 3.0 of the WRF model. The simulation was initialized at 00 UTC on 4 June 2005 using 1° Global Data Assimilation System analyses and then integrated for 24 h on a single 380 by 380 grid point domain containing 6 km horizontal resolution and 52 vertical levels. The vertical resolution decreased from less than 100 m in the lowest km to ~625 m at the model top, which was set to 25 hPa. Subgrid scale processes were parameterized using the *Thompson et al.* [2008] mixed phase cloud microphysics scheme, the Mellor-Yamada-Janjic planetary boundary layer scheme [*Mellor and Yamada*, 1982], and the *Dudhia* [1989] shortwave and rapid radiative transfer model [*Mlawer et al.*, 1997] longwave radiation schemes. Surface heat and moisture fluxes were calculated using the Noah land surface model. No cumulus parameterization scheme was used; therefore, all clouds were explicitly predicted by the microphysics scheme.

[13] The evolution of the simulated cloud top pressure (CTOP), cloud water path (CWP), and 300 hPa height and wind fields during the last 12 h of the simulation is shown in Figure 1. Simulated observations from this time period will be used in the assimilation experiments presented in section 4. The CWP was calculated using the sum of the cloud water, rainwater, ice, snow, and graupel mixing ratios integrated over the entire vertical column, whereas the CTOP represents the atmospheric pressure on the highest model level containing a nonzero hydrometeor mixing ratio. At 12 UTC, a deep upper-level trough was located over the central Rockies with a broad region of strong southwesterly flow across the southern Plains (Figure 1a). A large cirrus cloud shield with embedded regions of thicker stratiform and convective clouds was present across the northern Plains while extensive areas of low-level clouds were located over the eastern portion of the domain and along a surface cold front extending across the central Plains (Figure 1b). By 18 UTC, the 300 hPa winds had strengthened slightly over the central Plains as the trough continued to move toward the northeast (Figure 1c). Most of the low-level clouds had dissipated by this time, which resulted in an extensive area of clear skies across the southern half of the domain (Figure 1d). By 00 UTC, the circulation associated with the strong jet streak (not shown) had contributed to the development of an elongated cloud band extending from Texas to Iowa. Further north, the eastern portion of the cirrus cloud shield continued to move to the north and east while the western portion remained stationary. Taken together, the above demonstrate that the chosen case study contains a mixture of clear areas and an assortment of cloud

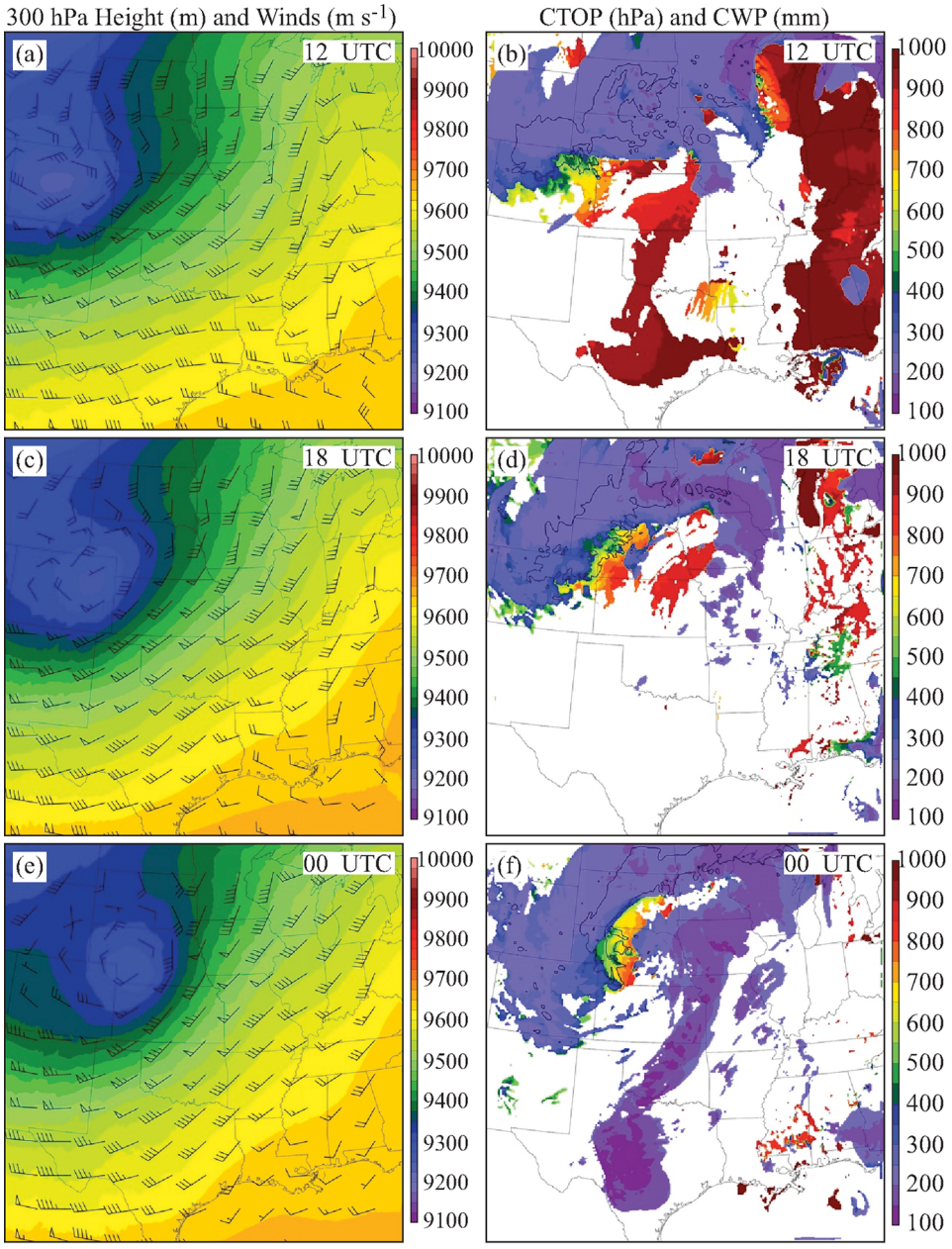

Figure 1. (a) Simulated 300 hPa geopotential height (m) and winds (m s^{-1}) valid at 1200 UTC on 4 June 2005. (b) Simulated cloud top pressure (hPa; color filled) valid at 1200 UTC on 4 June. Areas enclosed by the black contour contain a cloud water path greater than 0.5 mm. (c and d) Same as Figures 1a and 1b except valid at 1800 UTC on 4 June 2005. (e and f) Same as Figures 1a and 1b except valid at 0000 UTC on 5 June 2005.

types suitable for evaluating the impact of cloudy infrared radiances.

4. Assimilation Results

4.1. Initial Ensemble and Model Configuration

[14] The assimilation experiments described later in this section begin at 12 UTC on 4 June. A 40-member ensemble of initial conditions valid at this time was created using the following procedure. First, the approach outlined by *Torn et al.* [2006] was used to create an ensemble valid at 00 UTC on 3 June. With this approach, balanced initial and lateral boundary perturbations were added to 40 km North American Mesoscale (NAM) model analyses for each ensemble member using covariance information provided by the WRF-Var data assimilation system. This ensemble was then integrated for 24 h to increase the ensemble spread. Simulated radiosonde, ASOS, and ACARS observations from the truth simulation were then assimilated at 00 UTC on 4 June, with hourly assimilation of the ASOS and ACARS observations continuing until 12 UTC. This final step was used to produce an initial ensemble for the assimilation experiments con-

taining flow-dependent covariance structures representative of the atmospheric conditions in the truth simulation.

[15] Assimilation experiments were performed for the same geographic domain as the truth simulation. To better represent the grid resolution used in an operational setting, the model domain contained 12 km horizontal resolution and 37 vertical levels. Unlike the truth simulation, the Yonsei University [*Hong et al.*, 2006] planetary boundary layer scheme and the *Kain and Fritsch* [1990, 1993] cumulus scheme were employed. Different initialization data sets, grid resolutions, and parameterization schemes were chosen for the assimilation experiments to limit the risk of performing "identical twin" experiments.

[16] In the remainder of this section, results from four assimilation experiments and a control case without assimilation will be compared to data from the truth simulation. The experiments are designed to evaluate the relative impact of 8.5 μm infrared brightness temperatures, which are sensitive to cloud top properties when clouds are present or to the surface when clouds are absent, on the analysis accuracy. Both clear-sky and cloudy sky 8.5 μm brightness temperatures (ABI band 11) were assimilated in the "B11-ALL" case, whereas only the clear-sky brightness temperatures were assimilated in the "B11-CLEAR" case. Simulated conventional observations were assimilated in the "CONV" case. Finally, all of the conventional observations and both clear-sky and cloudy sky 8.5 μm brightness temperatures were assimilated in the "CONV-B11" case. Simulated radiosonde observations were assimilated at 00 and 12 UTC, whereas all other observation types were assimilated once per hour from 12 UTC on 4 June until 00 UTC on 5 June. Prognostic fields contained in the model state vector include the temperature, water vapor mixing ratio, horizontal and vertical wind components, surface pressure, number concentration of ice, and the mixing ratios for cloud water, rainwater, ice, snow, and graupel. The horizontal covariance localization radius was set to 255 km. Vertical localization was not used since infrared radiances are sensitive to an atmospheric layer that varies in the presence of clouds and with changes in the atmospheric state. The time and spatially varying inflation scheme developed by *Anderson et al.* [2009] was also used with the initial inflation factor set to 2%. The optimal settings for these parameters were determined using sensitivity tests employing the simulated observations.

4.2. Simulated Brightness Temperatures

[17] As a first step in evaluating the impact of the observations on the cloud distribution, simulated ABI 11.2 μm brightness temperatures from the assimilation experiments and the truth simulation are shown in Figure 2. The brightness temperatures for each assimilation case were computed using data from the posterior ensemble mean. As expected, the largest errors occur during the control simulation (Figures 2e–2h) since the lack of assimilation allows the ensemble spread to steadily increase, which manifests itself as a substantial cold bias and more extensive cloud cover by 00 UTC. Comparison of the B11-ALL (Figures 2i–2l) and B11-CLEAR (Figures 2m–2p) images reveals that infrared radiance assimilation has a much larger positive impact on the analysis when both clear-sky and cloudy sky observations are assimilated. For instance, though both cases contain fewer erroneous clouds over the southern portion of the domain due to the influence of the clear-sky radiances, the cloudy radiances were also able to correctly modify the overall structure of the cirrus cloud shield associated with the extratropical cyclone. The impact of the cloudy brightness temperatures is already evident after the first assimilation cycle by the narrower axis of the coldest cloud tops over the northwestern corner of the domain and the warmer brightness temperatures over Minnesota and Wisconsin (Figures 2e and 2i). Cloudy brightness temperature assimilation also resulted in a more accurate representation of the upper-level cloud cover that developed over central Texas by 00 UTC (Figures 2h and 2l). The conventional observations had a larger impact on these features (Figures 2q–2t) than the B11-CLEAR case but not as large as the B11-ALL case. These observations also had a smaller influence than the 8.5 μm radiances over the southern portion of the domain where much more extensive cloud cover developed by 00 UTC. Lastly, the CONV-B11 (Figures 2u–2x) and B11-ALL brightness temperatures are very similar across the entire domain though some differences exist such as the slightly colder cloud tops along the cold front by 00 UTC.

[18] To more closely examine the accuracy of the 00 UTC analyses, the 11.2 μm brightness temperature differences between the truth simulation and each assimilation experiment are shown in Figure 3. The 11.2 μm brightness temperatures from the truth simulation are also shown for reference. A detailed comparison of the B11-ALL, B11-CLEAR, and CONV cases (Figures 3c–3e) reveals that assimilating both clear-sky and cloudy sky 8.5 μm radiances generally produces a more accurate analysis across most of the domain than when only clear-sky radiances or conventional observations are assimilated. Though the conventional observations have a positive effect on the various cloudy areas relative to the control case (Figure 3b), the smaller errors found in the B11-ALL case indicate that explicit information about the cloud field provided by spatially continuous cloudy radiances is able to more easily constrain the cloud features within these regions. A notable discrepancy in all of the assimilation cases is the lack of enhanced upper-level cloud cover over northern Iowa, which was primarily due to the northward advection of erroneously dry air located over southern Iowa in the initial 12 UTC ensemble. The availability of conventional surface and upper-air moisture measurements in the CONV case slightly reduced the errors over this region by increasing the moisture content and producing a more favorable environment for cloud development. The 8.5 μm radiances, however, have little sensitivity to atmospheric water vapor and were therefore unable to improve the moisture analysis in this region. Clear areas across the southern half of the domain were generally better depicted in the B11-ALL and B11-CLEAR cases due to the strong constraint imposed on the cloud field by the clear-sky radiances. Much larger errors occurred when only conventional observations were assimilated, though the smaller errors relative to the control case indicate that some of the erroneous upper-level clouds were removed. Comparison of the B11-ALL and CONV-B11 images (Figures 3c and 3f) shows that the smallest brightness temperature errors were achieved when both conventional observations and clear-sky and cloudy sky 8.5 μm radiances were assimilated, which indicates that the moisture and thermodynamic information provided by conventional observations and the explicit cloud

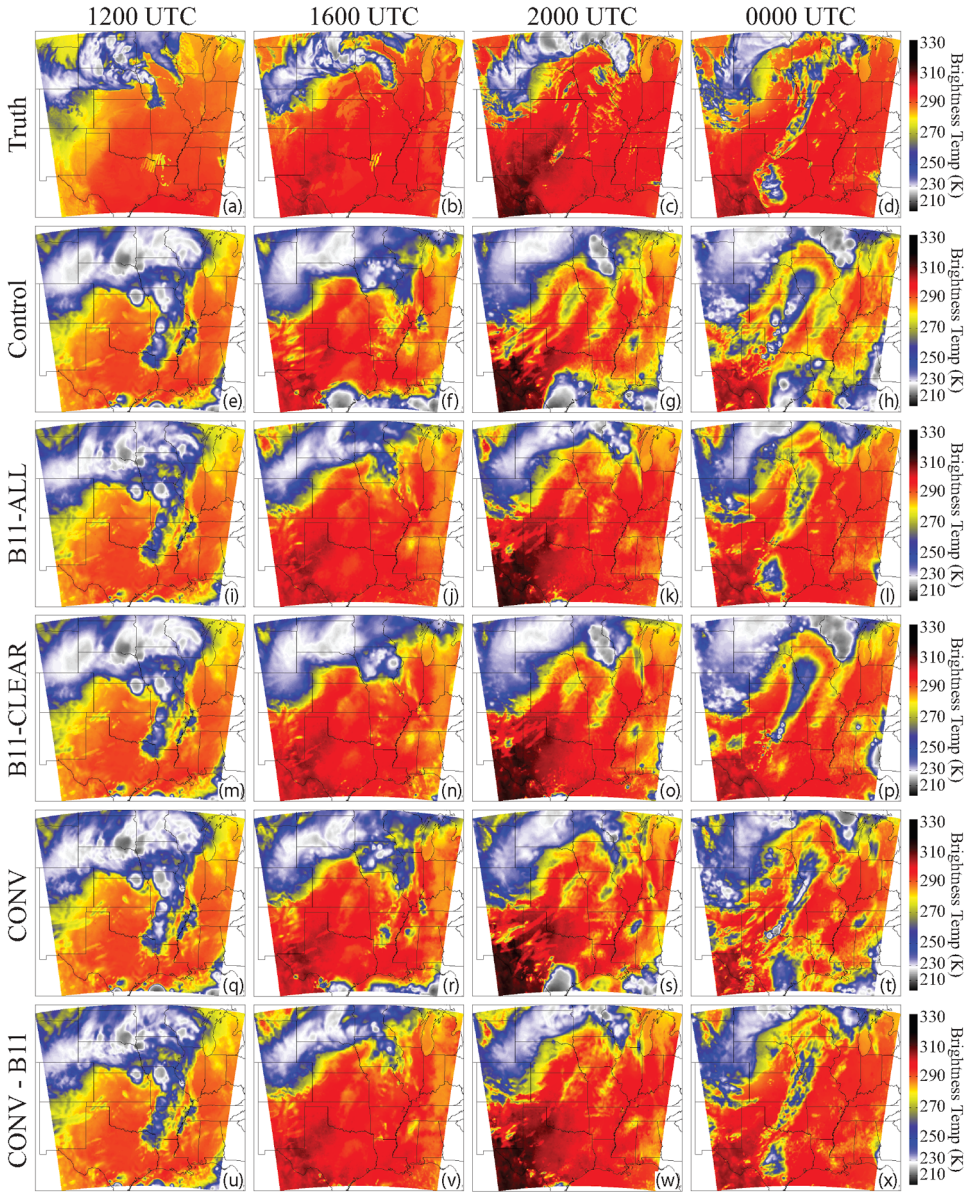

Figure 2. Simulated ABI 11.2 μm brightness temperatures (K) valid at 1200, 1600, and 2000 UTC on 4 June 2005 and 0000 UTC on 5 June 2005. Results are shown for the (a–d) truth and (e–h) control simulations and the (i–l) B11-ALL, (m–p) B11-CLEAR, (q–t) CONV, and (u–x) CONV-B11 assimilation experiments. The simulated brightness temperatures for each assimilation experiment were computed using data from the posterior ensemble mean.

information provided by 8.5 μm radiances can be synergistically combined to produce a more accurate cloud analysis.

[19] Figure 4 shows the temporal evolution of the forecast and analysis root mean square error (RMSE) and bias for the ABI 11.2 and 6.95 μm bands. Brightness temperatures from the 6.95 μm band are sensitive to the water vapor content in the middle and upper troposphere when upper-level clouds are not present. Data from the ensemble mean was interpolated from the coarser assimilation grid to the higher-resolution truth domain, and then statistics were computed with respect to the cloudy and clear grid points in the truth simulation. Data from the outermost 20 grid points were not used. Overall, it is evident that the B11-ALL and CONV-B11 cases contain the smallest bias and RMSE for both clear and cloudy grid points during the entire 12 h assimilation window. The greatest improvements were made to the analysis during the first several assimilation cycles, particularly for clear grid points, with nearly constant errors thereafter. Though the similar evolution of the B11-ALL and CONV-B11 cases demonstrates that the smaller errors were primarily due to the assimilation of 8.5 μm brightness temperatures, the slightly smaller errors present in the CONV-B11 case by 00 UTC indicate that the conventional observations provided additional information that further improved the analysis. The impact of the conventional observations is most apparent in the clear-sky 6.95 μm brightness temperatures, where the

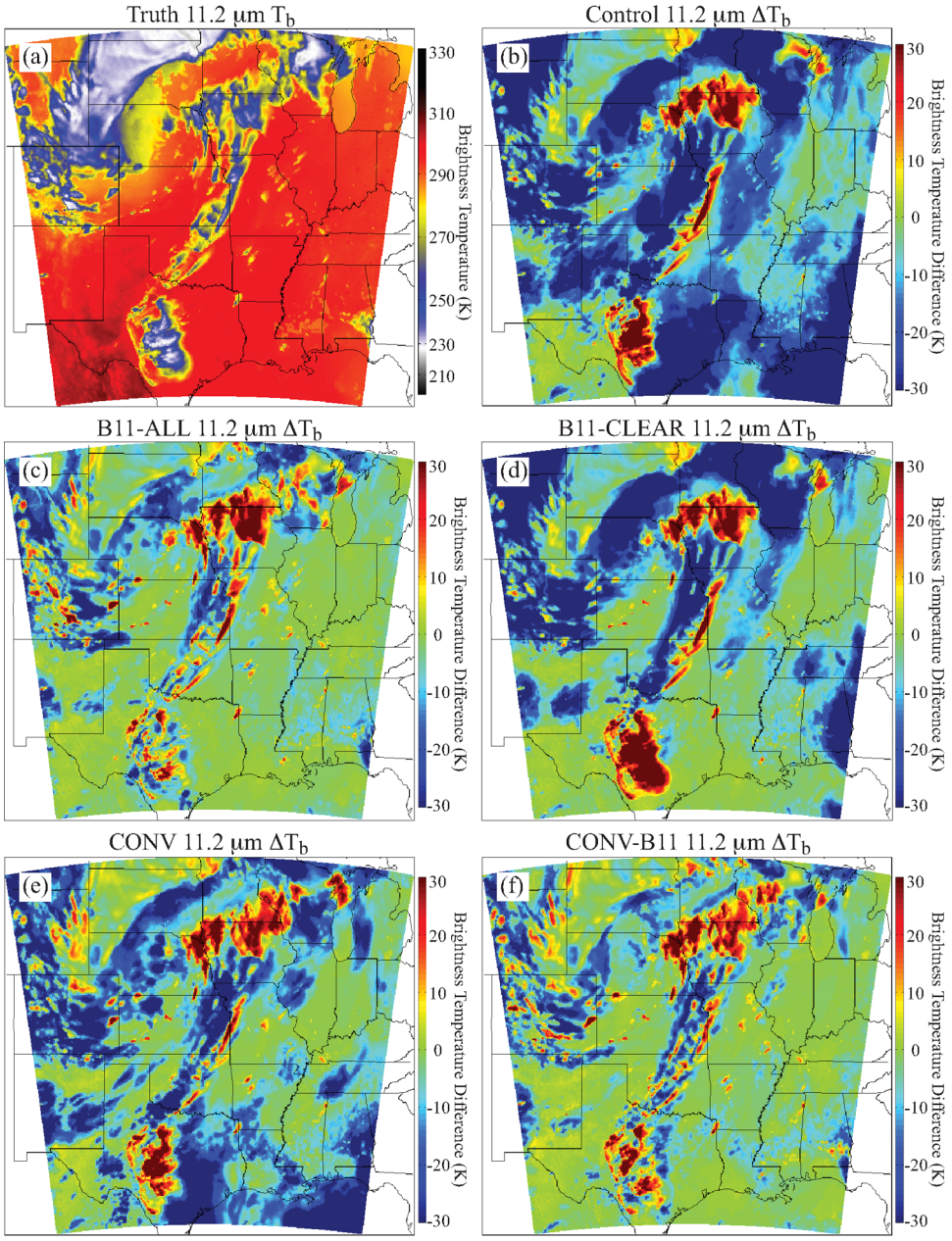

Figure 3. (a) Simulated ABI 11.2 μm brightness temperatures (K) from the truth simulation valid at 0000 UTC on 5 June 2005. (b) Control–Truth simulated ABI 11.2 μm brightness temperatures (K) valid at 0000 UTC on 5 June 2005. (c) Same as Figure 3b except for B11-ALL–Truth. (d) Same as Figure 3b except for B11-CLEAR–Truth. (e) Same as Figure 3b except for CONV–Truth. (f) Same as (b) except for CONV-B11–Truth. The simulated brightness temperatures for each assimilation experiment were computed using data from the posterior ensemble mean.

assimilation of drier surface and radiosonde moisture observations from the truth simulation reduced the wet bias that occurred in the assimilation experiments due to the use of a different initialization data set. By removing some of the excess water vapor, the 6.95 μm weighing function peaked at a lower (i.e., warmer) atmospheric level in the CONV-B11 case, which reduced the cold brightness temperature bias for the clear grid points. Lastly, comparison of the B11-CLEAR and CONV cases shows that the conventional observations reduced the errors by a slightly larger amount for the cloudy grid points but had a much smaller impact in clear areas.

4.3. Simulated Cloud Properties

[20] Figure 5 shows the evolution of the forecast and analysis RMSE and bias for the CWP and CTOP computed with respect to the cloudy and clear grid points in the truth simulation. To facilitate the comparison between clear and cloudy grid points, the surface pressure was used as the CTOP

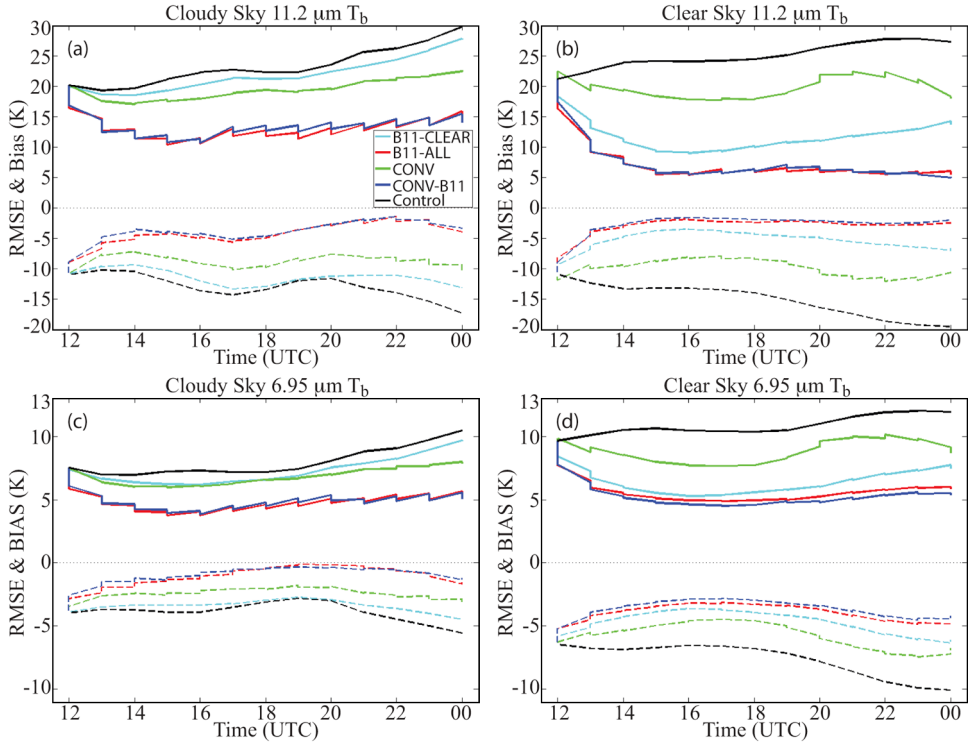

Figure 4. The time evolution of the forecast and analysis (sawtooth pattern) root mean square error (RMSE; thick solid lines) and bias (dashed lines) from 12 UTC on 4 June to 00 UTC on 5 June for the (a) cloudy and (b) clear ABI 11.2 μm brightness temperatures (K) and for the (c) cloudy and (d) clear ABI 6.95 μm brightness temperatures (K). Results are shown for the B11-CLEAR (light blue), B11-ALL (red), CONV (green), CONV-B11 (dark blue), and control (black) experiments, with the statistics calculated with respect to the cloudy and clear grid points in the truth simulation.

for the clear grid point. The evolution of the bias and RMSE for the cloudy sky CWP (Figure 5a) closely tracks the evolution of the control case during each assimilation experiment. Again, the B11-ALL and CONV-B11 cases contain the smallest errors, though by 00 UTC their RMSE is similar to the control case and the other assimilation experiments. All of the observation types have a much larger positive impact on the CWP for clear grid points (Figure 5b), with the 8.5 μm radiance assimilation cases generally performing better than the CONV case, especially after 16 UTC. This behavior is consistent with the removal of much of the erroneous upper-level cloud cover during these experiments (refer to Figures 2 and 3). Compared to the CWP statistics, the cloudy sky CTOP RMSE and bias (Figure 5c) underwent a more consistent and substantial improvement, particularly for the B11-ALL and CONV-B11 cases. Large improvements were also made to the clear-sky statistics during the B11-ALL, CONV-B11, and B11-CLEAR cases (Figure 5d). The presence of large CTOP errors in all of these experiments, however, is partially explained by how the statistics were computed. For instance, since it only takes one ensemble member with a nonzero mixing ratio for the ensemble mean to become cloudy, large errors can occur at the clear grid points even if most of the ensemble members are clear. Thus, the smaller errors during the radiance assimilation cases indicate that the 8.5 μm radiances were able to more easily remove the erroneous clouds from all of the ensemble members at more of the clear grid points than the conventional observations.

[21] Figure 6 shows the geographic distribution of the CWP differences between the truth simulation and each assimilation experiment at 00 UTC. Overall, the largest errors are located within or close to regions containing large CWP, such as the northern portion of the domain and along the cold front (Figure 6a). CWP errors within the northern cloud shield were substantially reduced when cloudy sky 8.5 μm brightness temperatures and conventional observations were assimilated. Compared to the CONV case, cloudy sky brightness temperature assimilation tended to produce a more accurate analysis across much of this region, though the north-south band of excessive CWP within the center of the cloud shield indicates that their utility is limited for clouds containing substantial condensate. Further south, the cloudy 8.5 μm observations reduced the CWP along the cold front while increasing it within the area of enhanced cloudiness over central Texas, in both cases producing a more accurate analysis than when only conventional or clear-sky 8.5 μm brightness temperature observations were assimilated.

[22] To examine the impact on the vertical distribution of cloud condensate, Figure 7 shows RMSE and bias profiles for the frozen (FRZN) and liquid (LIQ) hydrometeor mixing ratios computed with respect to the clear and cloudy grid points in the truth simulation. The FRZN mixing ratio is the sum of the cloud ice, snow, and graupel species, whereas the LIQ mixing ratio is the sum of the cloud water and rainwater species. The statistics were calculated for each assimilation

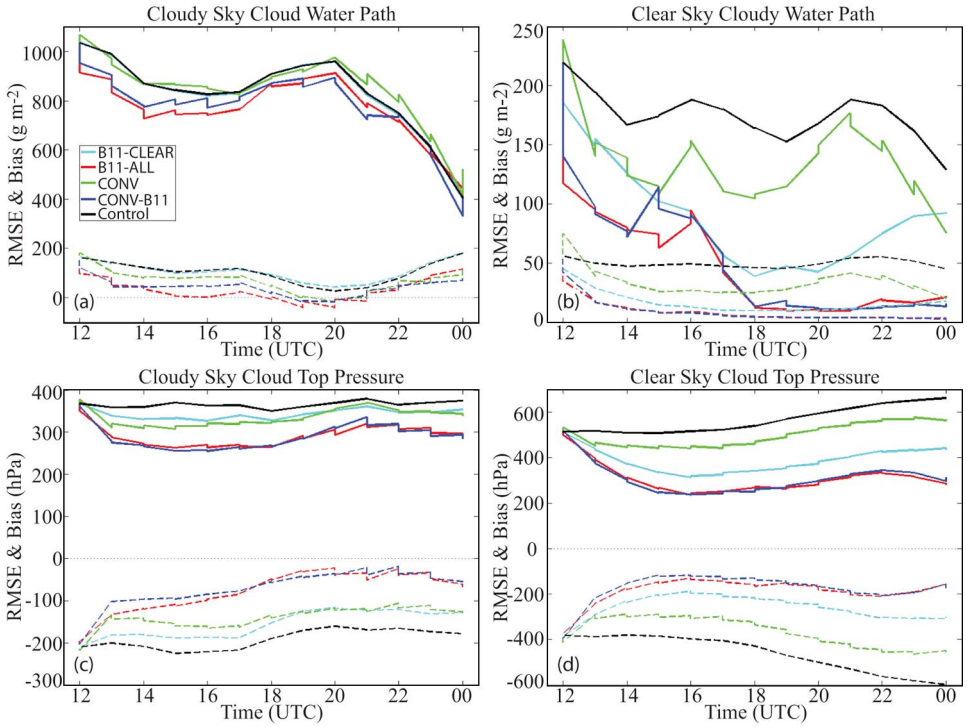

Figure 5. The time evolution of the forecast and analysis (sawtooth pattern) root mean square error (RMSE; thick solid lines) and bias (dashed lines) from 12 UTC on 4 June to 00 UTC on 5 June for the (a) cloudy sky and (b) clear-sky cloud water path (g m^{-2}) and for the (c) cloudy sky and (d) clear-sky cloud top pressure (hPa). Results are shown for the B11-CLEAR (light blue), B11-ALL (red), CONV (green), CONV-B11 (dark blue), and control (black) experiments, with the statistics calculated with respect to the cloudy and clear grid points in the truth simulation.

case using data from the prior ensemble mean from 13 UTC on 4 June until 00 UTC on 5 June.

[23] Comparison of the CONV, B11-ALL, and B11-CLEAR profiles shows that the cloudy sky 8.5 μm brightness temperatures were the only observations that reduced the FRZN RMSE and bias for the cloudy grid points (Figure 7a). The smaller errors in both the middle and upper troposphere indicate that cloud information provided by the infrared radiances improves not only the cloud top but also the internal structure of the simulated clouds even though the radiance observations are only sensitive to the uppermost portion of the cloud. Inspection of the model data (not shown) revealed that the smaller errors were primarily due to a more accurate representation of the snow mixing ratio, which is the dominant species in the Thompson microphysics scheme. Each observation type substantially reduced the RMSE and bias for the clear-sky grid points (Figure 7b), though the radiance assimilation cases exhibit the smallest errors overall. In fact, nearly all of the FRZN cloud condensate was removed during the B11-ALL case. The smaller errors for this case also indicate that cloudy radiances not only improve the cloud analysis in the cloudy portion of the domain but also exert a positive influence on adjacent clear regions, most likely through a more accurate depiction of the cloud morphology. For the liquid portion of the cloud field (Figures 7c and 7d), the conventional observations have the tendency to degrade the cloud analysis in both clear and cloudy areas while the 8.5 μm brightness temperatures have minimal impact in cloudy areas and a slightly positive impact on the clear grid points. It is suggested that the smaller impact of the infrared radiances on the LIQ mixing ratio compared to the FRZN mixing ratio is due either to obscuration of the lower portion of the cloud by upper-level clouds or to smaller observation minus background differences due to the lack of thermal contrast between low clouds and the surface, which reduces the magnitude of the analysis increment.

4.4. Simulated Thermodynamic Profiles

[24] Vertical profiles of RMSE and bias for the atmospheric water vapor, temperature, and horizontal wind magnitude are shown in Figure 8. The statistics were calculated using data from the prior ensemble mean from 13 UTC on 4 June until 00 UTC on 5 June. Large water vapor mixing ratio errors are generally present in all the assimilation cases for both clear and cloudy grid points (Figures 8a and 8b). The large errors in the upper levels were primarily due to the higher water vapor content in the initialization data set used during the assimilation experiments (not shown) while large differences in the vertical water vapor flux profiles produced by the planetary boundary layer schemes contributed to the large errors in the lower troposphere. In most cases, however, small improvements were made to the water vapor analysis, with the B11-ALL case containing smaller errors in the middle and upper troposphere than the other cases.

[25] Similar temperature error profiles occurred for both clear and cloudy grid points during each assimilation exper-

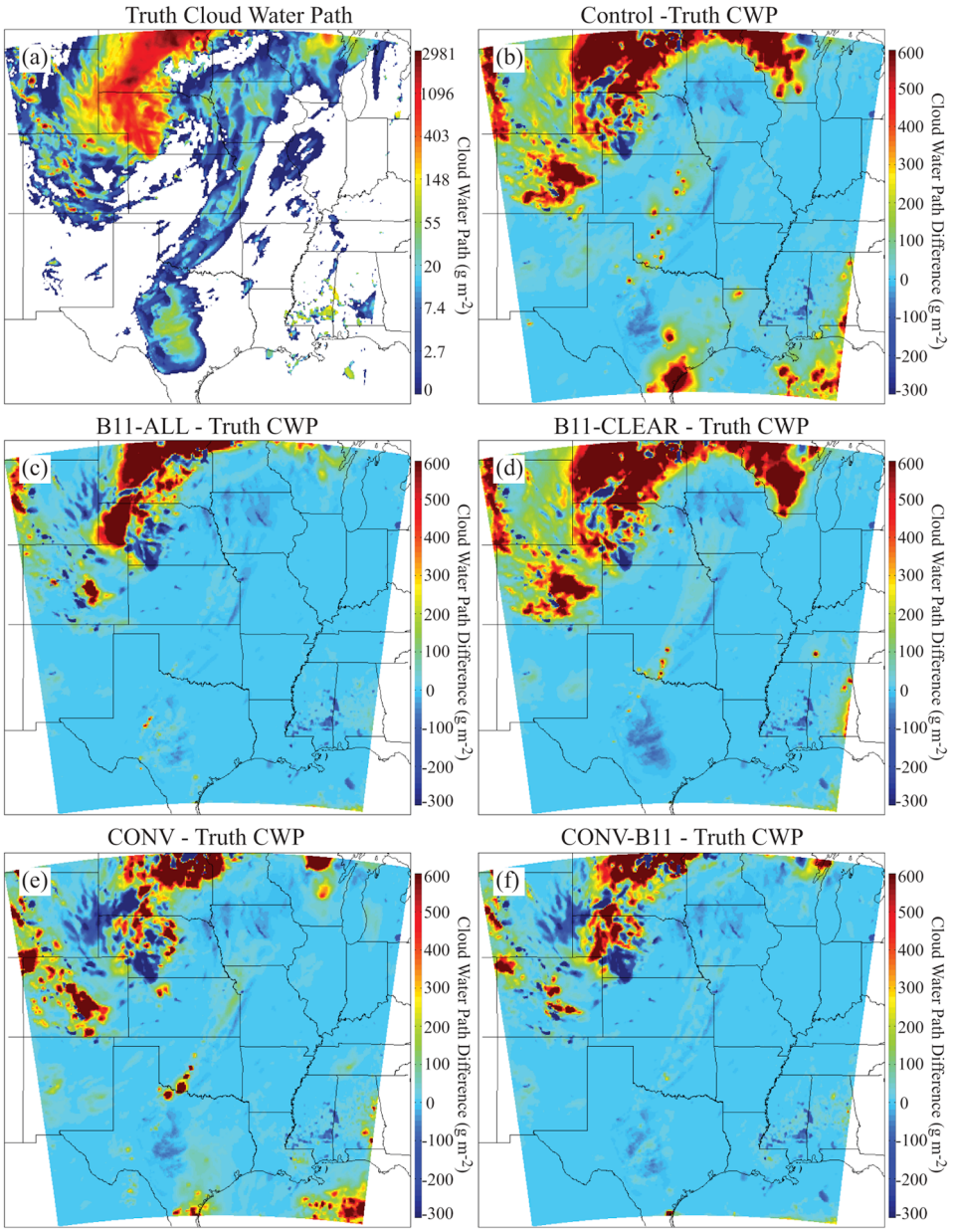

Figure 6. (a) Simulated cloud water path (CWP; g m^{-2}) from the truth simulation valid at 0000 UTC on 5 June 2005. (b) Control–Truth simulated CWP (g m^{-2}) valid at 0000 UTC on 5 June 2005. (c) Same as Figure 6b except for B11-ALL–Truth. (d) Same as Figure 6b except for B11-CLEAR–Truth. (e) Same as Figure 6b except for CONV–Truth. (f) Same as Figure 6b except for CONV-B11–Truth. The simulated CWP for each assimilation experiment was computed using data from the posterior ensemble mean.

iment (Figures 8c and 8d). The large error spike near 150 hPa was primarily due to different locations in the height and structure of the tropopause while the larger errors in the lower troposphere were partially caused by different behavior in the planetary boundary layer schemes. Aside from these basic differences, it is evident that the CONV case generally contains the smallest errors though the CONV-B11 errors are slightly smaller in the upper troposphere. Infrared radiance assimilation reduced the temperature errors in the upper troposphere but had little positive impact or even slightly degraded the analysis below 500 hPa. Similar behavior is also observed in the wind magnitude error profiles (Figures 8e and 8f) where the CONV and CONV-B11 cases generally contain the smallest errors. Radiance assimilation did not improve the wind analysis within clear areas of the domain; however, the errors were substantially reduced above 700 hPa for cloudy grid points when cloudy infrared radiances were assimilated. The tendency for the cloudy observations to improve the analysis at cloudy grid points indicates that these observations contain sufficient covariance information to improve the wind, temperature, and moisture fields, particularly in the upper troposphere. The inability of the clear-sky observations to exert a similar influence on these fields, however, may be due to the lack of implicit height information, which may help

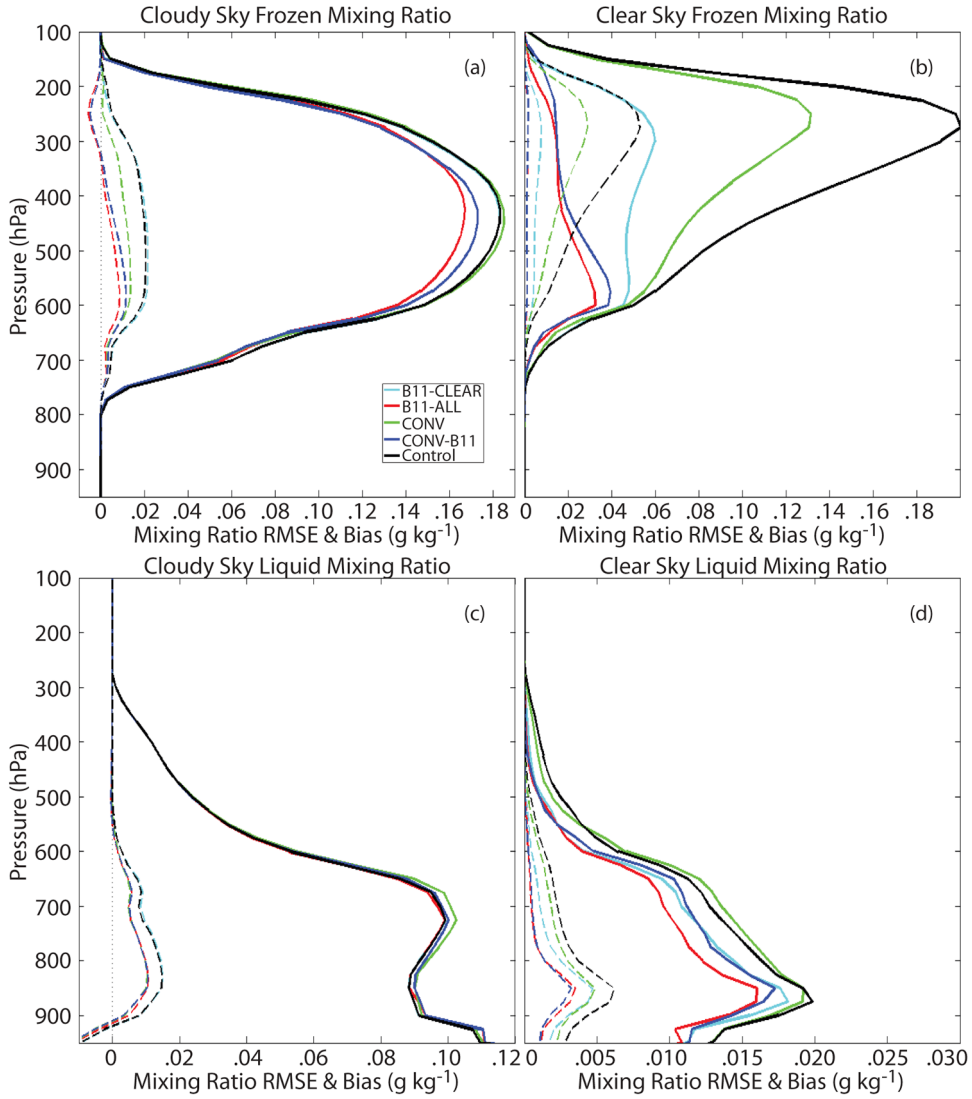

Figure 7. (a) Vertical profiles of root mean square error (RMSE; thick solid lines) and bias (dashed lines) for the total frozen hydrometeor mixing ratio (g kg^{-1}; sum of cloud ice, snow, and graupel) for cloudy grid points. The profiles were computed using data from the prior ensemble mean from 1300 UTC on 4 June to 0000 UTC on 5 June. (b) Same as Figure 7a except for clear grid points. (c) Same as Figure 7a except for the total liquid hydrometeor mixing ratio (g kg^{-1}; sum of cloud water and rainwater). (d) Same as Figure 7c except for clear grid points. Results are shown for the B11-CLEAR (light blue), B11-ALL (red), CONV (green), CONV-B11 (dark blue), and control (black) experiments, with the statistics calculated with respect to the cloudy and clear grid points in the truth simulation.

constrain the covariances around the cloud top for cloudy observations. The full impact of the infrared observations may become more apparent with a longer assimilation window since the feedback between these fields would have more time to develop.

5. Discussion and Conclusions

[26] In this study, a regional-scale OSSE was used to examine how the assimilation of infrared brightness temperatures for both clear-sky and cloudy sky conditions impacts the accuracy of atmospheric analyses at mesoscale resolution. Assimilation experiments were conducted using the EnKF algorithm in the DART data assimilation system. The SOI forward radiative transfer model was implemented in DART to assimilate infrared brightness temperature observations. The case study tracked the evolution of a large extratropical cyclone and associated cloud features present across the central United States during 4–5 June 2005. A high-resolution "truth" simulation containing realistic cloud and thermodynamic properties was performed using the WRF model. Data from the truth simulation was used to generate simulated GOES-R ABI 8.5 μm brightness temperatures and conventional radiosonde, surface, and aircraft pilot observations containing realistic errors and the correct spatial distribution. Four assimilation experiments were conducted with observations assimilated once per hour during a 12 h period.

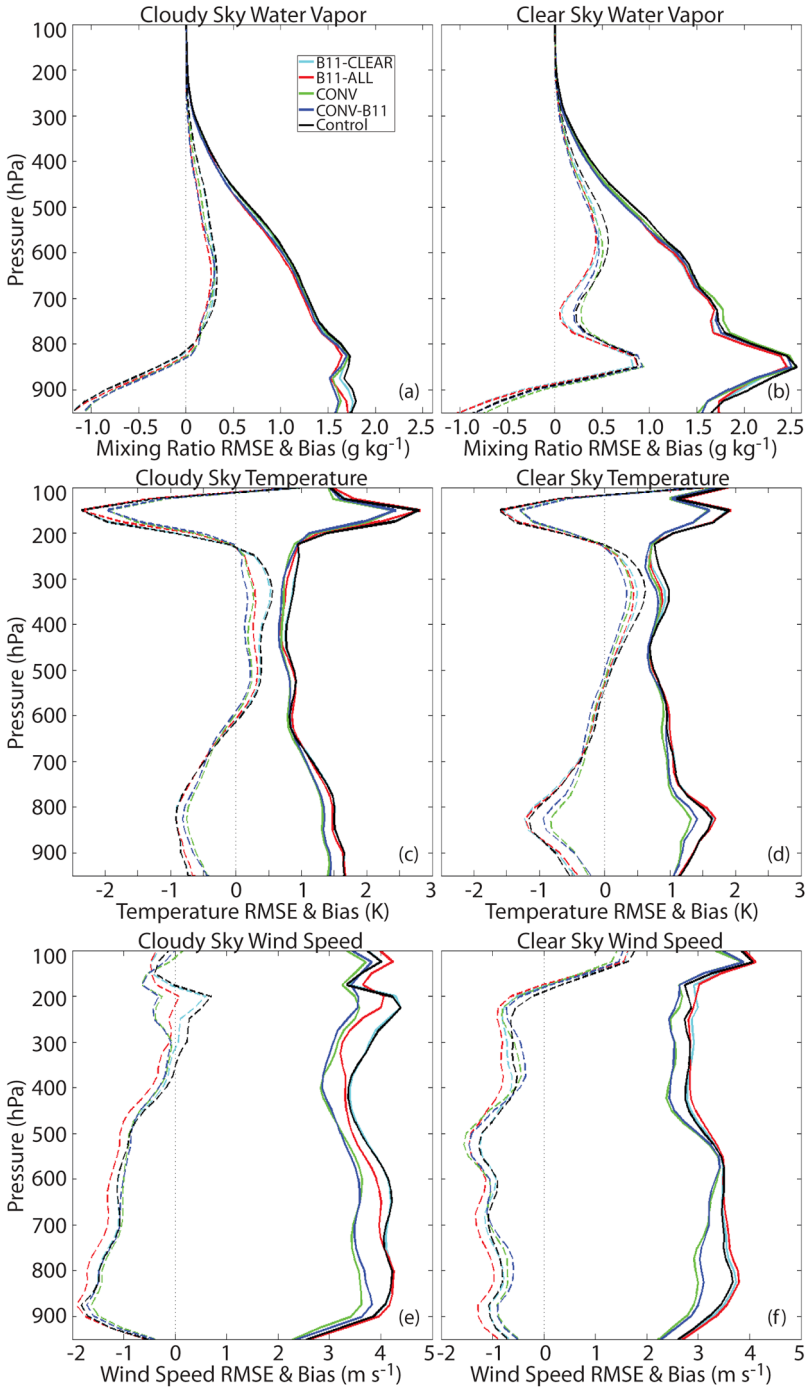

Figure 8. (a) Vertical profiles of root mean square error (RMSE; thick solid lines) and bias (dashed lines) for the water vapor mixing ratio (g kg^{-1}) for cloudy grid points. The profiles were computed using data from the prior ensemble mean from 1300 UTC on 4 June to 0000 UTC on 5 June. (b) Same as Figure 8a except for clear grid points. (c) Same as Figure 8a except for temperature (K). (d) Same as Figure 8c except for clear grid points. (e) Same as Figure 8a except for wind speed (m s^{-1}). (f) Same as Figure 8e except for clear grid points. Results are shown for the B11-CLEAR (light blue), B11-ALL (red), CONV (green), CONV-B11 (dark blue), and control (black) experiments, with the statistics calculated with respect to the cloudy and clear grid points in the truth simulation.

[27] Overall, the assimilation results showed that the infrared brightness temperature observations had a large positive impact on the simulated cloud field with the best results achieved when both clear-sky and cloudy sky observations were assimilated. The B11-ALL and B11-CLEAR cases contained fewer erroneous upper level clouds over the southern portion of the model domain than the CONV case due to the strong constraint imposed on the cloud field by the

clear-sky brightness temperatures. Further north, assimilation of the cloudy brightness temperatures substantially improved the structure of the cyclone's cirrus cloud shield, with much smaller errors already apparent after the first assimilation cycle. The cloudy observations also improved the representation of the upper-level clouds that developed over central Texas and along the surface cold front by the end of the assimilation period. The ability of the infrared brightness temperatures to improve the cloud analysis was further demonstrated by the substantially lower bias and RMSE in the CTOP, CWP, 6.95 and 11.2 μm brightness temperatures, and vertical profiles of cloud condensate. When computed with respect to the cloudy and clear grid points in the truth simulation, the largest error reductions generally occurred within clear areas due to the removal of much of the erroneous cloud cover, though the errors were also greatly reduced in cloudy regions. The cloudy infrared brightness temperatures were the only observations that reduced the cloud condensate errors in the upper troposphere for the cloudy grid points, which indicates that the cloud information provided by infrared brightness temperatures not only improves the cloud distribution but also exerts some indirect influence on the internal structure of the simulated clouds. Because of this influence, it is also possible that cloudy infrared observations have the potential to reduce forecast error growth by partially constraining important cloud and precipitation processes, such as latent heat release associated with condensation and deposition, that can contribute to fast error growth in numerical models. This topic will be addressed in future studies.

[28] Inspection of the thermodynamic statistics revealed that the assimilation of conventional surface and upper air observations produced more accurate temperature and wind analyses than the B11-ALL and B11-CLEAR cases, especially for clear grid points. The impact on the water vapor mixing ratio varied with height, with the conventional moisture observations contributing to a more accurate analysis in the lower troposphere while the more accurate cloud field in the B11-ALL and B11-CLEAR cases helped constrain the errors above 800 hPa. When both cloud-affected and thermodynamic variables are considered, however, the CONV-B11 case generally performed best since its errors were similar to the B11-ALL case for the cloud variables and to the CONV case for the thermodynamic variables, which indicates that the best analysis is achieved when conventional observations and clear and cloud sky 8.5 μm brightness temperatures are assimilated together. Lastly, the tendency for the B11-ALL and B11-CLEAR cases to contain smaller errors for the cloud-affected fields, but slightly larger errors for more traditional measures of analysis accuracy such as temperature and wind, illustrates that the notable benefits of assimilating cloudy observations can be missed and are difficult to verify without the availability of high-quality cloud analyses and in situ measurements.

[29] **Acknowledgments.** This work was funded by the NOAA/NESDIS GOES-R Risk Reduction Program grant NA06NES4400002. Special thanks are given to Nancy Collins and Yongsheng Chen for their DART support and for providing scripts to run the data assimilation system. Thanks are also given to Will Lewis and Tom Greenwald for many valuable discussions. Comments from three anonymous reviewers helped improve the manuscript.

References

Anderson, J. L. (2001), An ensemble adjustment Kalman filter for data assimilation, *Mon. Weather Rev.*, *129*, 2884–2903.

Anderson, J. L. (2007), An adaptive covariance inflation error correction algorithm for ensemble filters, *Tellus*, *59A*, 210–224.

Anderson, J. L. (2009), Spatially and temporally varying adaptive covariance inflation for ensemble filters, *Tellus*, *61A*, 72–83.

Anderson, J., T. Hoar, K. Raeder, H. Liu, N. Collins, R. Torn, and A. Avellano (2009), The Data Assimilation Research Testbed: A community facility, *Bull. Am. Meteorol. Soc.*, *90*, 1283–1296.

Andersson, E., A. Hollingsworth, G. Kelly, P. Lonnberg, J. Pailleaux, and Z. Zhang (1991), Global observing system experiments on operational statistical retrievals of satellite sounding data, *Mon. Weather Rev.*, *119*, 1851–1864.

Baum, B. A., P. Yang, A. J. Heymsfield, S. Platnick, M. D. King, Y.-X. Hu, and S. T. Bedka (2006), Bulk scattering properties for the remote sensing of ice clouds: Part II. Narrowband models, *J. Appl. Meteorol.*, *44*, 1896–1911.

Bouttier, F., and G. Kelly (2001), Observing-system experiments in the ECMWF 4D-Var data assimilation system, *Q. J. R. Meteorol. Soc.*, *127*, 1469–1488.

Chevallier, F., P. Lopez, A. M. Tompkins, M. Janiskova, and E. Moreau (2004), The capability of 4D-Var systems to assimilate cloud-affected satellite infrared radiances, *Q. J. R. Meteorol. Soc.*, *130*, 917–932.

Collard, A. D., and A. P. McNally (2009), The assimilation of Infrared Atmospheric Sounding Interferometer radiances at ECMWF, *Q. J. R. Meteorol. Soc.*, *135*, 1044–1058, doi:10.1002/qj.410

Derber, J. C., and W.-S. Wu (1998), The use of TOVS cloud-cleared radiances in the NCEP SSI analysis system, *Mon. Weather Rev.*, *126*, 2287–2299.

Dudhia, J. (1989), Numerical study of convection observed during the winter monsoon experiment using a mesoscale two-dimensional model, *J. Atmos. Sci.*, *46*, 3077–3107.

Errico, R. M., P. Bauer, and J.-F. Mahfour (2007), Issues regarding the assimilation of cloud and precipitation data, *J. Atmos. Sci.*, *64*, 3785–3798.

Evensen, G. (1994), Sequential data assimilation with a nonlinear quasi-geostrophic model using Monte Carlo methods to forecast error statistics, *J. Geophys. Res.*, *99*(C5), 10143–10162, doi:10.1029/94JC00572.

Gaspari, G., and S. E. Cohn (1999), Construction of correlation functions in two and three dimensions, *Q. J. R. Meteorol. Soc.*, *125*, 723–757.

Halem, M., E. Kalnay, W. E. Baker, and R. Atlas (1982), An assssment of the FGGE satellite observing system during SOP-1, *Bull. Am. Meteorol. Soc.*, *63*, 407–429.

Hamill, T. M., J. S. Whitaker, and C. Snyder (2001), Distance-dependent filtering of background error covariance estimates in an ensemble Kalman filter, *Mon. Weather Rev.*, *129*, 2776–2790.

Han, Q., W. Rossow, R. Welch, A. White, and J. Chou (1995), Validation of satellite retrievals of cloud microphysics and liquid water path using observations from FIRE, *J. Atmos. Sci.*, *52*, 4183–4195.

Heidinger, A. K., C. O'Dell, R. Bennartz, and T. Greenwald (2006), The successive-order-of-interaction radiative transfer model: Part I. Model development, *J. Appl. Meteorol. Clim.*, *45*, 1388–1402.

Heillette, S., and L. Garand (2007), A practical approach for the assimilation of cloudy infrared radiances and its evaluation using AIRS simulated observations, *Atmos. Ocean*, *45*, 211–225.

Heymsfield, A. J., S. Matrosov, and B. Baum (2003), Ice water path–optical depth relationships for cirrus and deep stratiform ice cloud layers, *J. Appl. Meteorol.*, *42*, 1369–1390.

Hong, S.-Y., Y. Noh and J. Dudhia (2006), A new vertical diffusion package with an explicit treatment of entrainment processes, *Mon. Weather Rev.*, *134*, 2318–2341.

Kain, J. S., and J. M. Fritsch (1990), A one-dimensional entraining detraining plume model and its application in convective parameterization, *J. Atmos. Sci.*, *47*, 2784–2802.

Kain, J. S., and J. M. Fritsch (1993), Convective parameterization for mesoscale models: The Kain-Fritsch scheme, in *The representation of cumulus convection in numerical models*, K. A. Emanuel and D. J. Raymond (Eds.), 246 pp., Am. Meteorol. Soc

Le Marshall, J., et al. (2006), Improving global analysis and forecasting with AIRS, *Bull. Am. Meteorol. Soc.*, *87*, 891–894, doi:10.1175/BAMS-87-7-891.

McCarty, W., G. Jedloveck, and T. L. Miller (2009), Impact of the assimilation of Atmospheric Infrared Sounder radiance measurements on short-term weather forecasts, *J. Geophys. Res.*, *114*, D18122, doi:10.1029/2008JD011626.

McNally, A. P. (2009), The direct assimilation of cloud-affected satellite infrared radiances in the ECMWF 4D-Var, *Q. J. R. Meteorol. Soc.*, *135*, 1214–1229.

McNally, A. P., J. C. Derber, W. Wu, and B. B. Katz (2000), The use of TOVS level-1b radiances in the NCEP SSI analysis system, *Q. J. R. Meteorol. Soc.*, *126*, 689–724, doi:10.1002/qj.49712656315.

McNally, A. P., P. D. Watts, J. A. Smith, R. Engelen, G. A. Kelly, J. N. Thepaut, and M. Matricardi (2006), The assimilation of AIRS radiance data at ECMWF, *Q. J. R. Meteorol. Soc.*, *132*, 935–957.

Mellor, G. L., and T. Yamada (1982), Development of a turbulence closure model for geophysical fluid problems, *Rev. Geophys. Space Phys.*, *20*, 851–875.

Mitchell, H. L., P. L. Houtekamer, and G. Pellerin (2002), Ensemble size, balance, and model-error representation in an ensemble Kalman filter, *Mon. Weather Rev.*, *130*, 2791–2808.

Mlawer, E. J., S. J. Taubman, P. D. Brown, and M. J. Iacono (1997), Radiative transfer for inhomogeneous atmospheres: RRTM, a validated correlated-k Model for the longwave, *J. Geophys. Res.*, *102*, 16663–16682, doi:10.1029/97JD00237.

Mo, K. C., X. L. Wang, R. Kistler, M. Kanamitsu, and E. Kalnay (1995), Impact of satellite data on the CDAS-reanalysis system, *Mon. Weather Rev.*, *123*, 124–139.

O'Dell, C. W., A. K. Heidinger, T. Greenwald, P. Bauer, and R. Bennartz (2006), The successive-order-of-interaction radiative transfer model: Part II. Model performance and applications, *J. Appl. Meteorol. Climatol.*, *45*, 1403–1413.

Otkin, J. A., and T. J. Greenwald (2008), Comparison of WRF model-simulated and MODIS-derived cloud data, *Mon. Weather Rev.*, *136*, 1957–1970.

Otkin, J. A., T. J. Greenwald, J. Sieglaff, and H.-L. Huang (2009), Validation of a large-scale simulated brightness temperature data set using SEVIRI satellite observations, *J. Appl. Meteorol. Climatol.*, *48*, 1613–1626.

Reale, O., J. Susskind, R. Rosenbert, E. Brin, E. Liu, L. P. Riishojgaard, J. Terry, and J. C. Jusem (2008), Improving forecast skill by assimilation of quality-controlled AIRS temperature retrievals under partially cloudy conditions, *Geophys. Res. Lett.*, *35*, L08809, doi:10.1029/2007GL033002.

Schmit, T. J., M. M. Gunshor, W. P. Menzel, J. J. Gurka, J. Li, and A. S. Bachmeier (2005), Introducing the next-generation Advanced Baseline Imager on GOES-R, *Bull. Am. Meteorol. Soc.*, *86*, 1079–1096.

Seeman, S. W., E. E. Borbas, R. O. Knuteson, G. R. Stephenson, and H.-L. Huang (2008), Development of a global infrared land surface emissivity data base for application to clear sky sounding retrievals from multispectral satellite radiance measurements, *J. Appl. Meteorol. Climatol.*, *47*, 108–123.

Skamarock, W. C., J. B. Klemp, J. Dudhia, D. O. Gill, D. M. Barker, W. Wang, and J. G. Powers (2005), A description of the Advanced Research WRF Version 2, *NCAR Tech. Note/TN-468+STR*, 88 pp.

Thompson, G., P. R. Field, R. M. Rasmussen, and W. D. Hall (2008), Explicit forecasts of winter precipitation using an improved bulk microphysics scheme: Part II. Implementation of a new snow parameterization, *Mon. Weather Rev.*, *136*, 5095–5115.

Torn, R. D., G. J. Hakim, and C. Snyder (2006), Boundary conditions for limited-area ensemble Kalman filters, *Mon. Weather Rev.*, *134*, 2490–2502.

Tracton, M. S., A. J. Desmarais, R. J. van Haaren, and R. D. McPherson (1980), The impact of satellite soundings on the National Meteorological Center's analysis and forecast system – The data systems test results, *Mon. Weather Rev.*, *108*, 543–586.

Vukicevic, T., T. Greenwald, M. Zupanski, D. Zupanski, T. Vonder Haar, and A. Jones (2004), Mesoscale cloud state estimation from visible and infrared satellite radiances, *Mon. Weather Rev.*, *132*, 3066–3077.

Vukicevic, T., M. Sengupta, A. S. Jones, and T. Vonder Haar (2006), Cloud-resolving satellite data assimilation: Information content of IR window observations and uncertainties in estimation, *J. Atmos. Sci.*, *63*, 901–919.

Whitaker, J. S., and T. M. Hamill (2002), Ensemble data assimilation without perturbed observations, *Mon. Weather Rev.*, *130*, 1913–1924.

Xu, J., S. Rugg, L. Byerle, and Z. Liu (2009), Weather Forecasts by the WRF-ARW model with GSI data assimilation system in complex terrain areas of southwest Asia, *Weather Forecasting*, *24*, 987–1008, doi:10.1175/2009WAF2222229.1.

Zupanski, D., M. Zupanski, L. D. Grasso, R. Brummer, I. Jankov, D. Lindsey, M. Sengupta, and M. DeMaria (2010), Assimilating synthetic GOES-R radiances in cloudy conditions using an ensemble-based method, *Int. J. Remote Sens.*, in press.

J. A. Otkin, Cooperative Institute for Meteorological Satellite Studies, University of Wisconsin-Madison, 1225 W. Dayton St., Madison, WI 53706, USA. (jasono@ssec.wisc.edu)